Energy Storage Materials 59 (2023) 102764

Contents lists available at ScienceDirect

Energy Storage Materials

journal homepage: www.elsevier.com/locate/ensm

Engineering d-band center of FeN_4 moieties for efficient oxygen reduction reaction electrocatalysts

Zheng Li [a], Zhongliang Tian [a,*], Hao Cheng [a], Tao Wang [a], Wei Zhang [b], Yao Lu [a], Yanqing Lai [a,*], Guanjie He [b,*]

[a] School of Metallurgy and Environment, Central South University, Changsha 410083, China
[b] Hubei Christopher Ingold Laboratory, Department of Chemistry, University College London, 20 Gordon Street, London WC1H 0AJ, UK

ARTICLE INFO

Keywords:
D-band center upshift
Fe-Zn atomic pair
Oxygen reduction reaction
Metal-air battery

ABSTRACT

Atomically-dispersed FeN_4 moieties are emerging as low-cost electrocatalysts for oxygen reduction reaction (ORR), which can be applied in fuel cells and metal-air batteries. Whereas, the unsatisfactory position of the d-band center from the metal sites offered by FeN_4 affects the adsorption-desorption behaviors of oxygenated intermediates, further impeding the improvement of their ORR performances. Herein, we report a well-designed diatomic Fe/Zn-CNHC catalyst on a microporous hollow support. This strategy drives the position of the d-band center of Fe upward, thus making FeN_4 active sites more favorable and stable during the ORR kinetic processes. The material exhibits an excellent ORR activity with a half-wave potential of 0.91 V and excellent stability (insignificant attenuation after 5,000 cycles), surpassing commercial Pt/C and many other single-atom catalysts. DFT calculations further indicate that the tuning effect of Zn on the d-orbital electron distribution of Fe facilitates the stretching and cleavage of Fe-O, thus accelerating the rate-determining step. This work presents a simple strategy to fabricate well-defined diatomic coordination in single-atom ORR electrocatalysts and inspires future research on developing new syntheses to control the coordination of single-atom electrocatalysts.

1. Introduction

Fuel cells and metal-air batteries are regarded as viable next-generation sustainable energy solutions for effectively mitigating global warming and achieving carbon neutrality [1–5]. Though Pt-based catalysts exhibit excellent O_2 adsorption and catalytic activity for oxygen reduction reaction (ORR), the high cost and low reserve sternly restrict their large-scale applications [6–10]. Exploring earth-abundant and cost-effective non-Pt ORR catalysts with high activity and stability is crucial for promoting the commercialization of these energy technologies [11–13]. Single-atom catalysts (SACs) with the structure of isolated transition metal-nitrogen-carbon have been considered the most promising candidate to replace platinum group metals (PGM) for catalyzing ORR, due to their decent catalytic activity and stability in acid/alkaline electrolytes [14–17]. Fe-Nx/C molecules exhibit overall similar ORR activity compared to other M-Nx/C counterparts because of the adsorption energies of O_2 molecules and thermodynamically favorable $4e^-$ pathway [18]. However, further research revealed that the strong electronegativity of N atoms enabled metal sites to strongly bind with electron-donating intermediates, leading to high energy barriers for the subsequent desorption steps, and thus need further modification. In addition, there is still a need for a better understanding of the modulation of the electronic structures of Fe-N-C catalysts to further reduce the overpotential and improve the kinetic activity [19–23]. d-band center (E_d) is considered an efficient descriptor for the electronic structure of transition metal-based catalysts, which can reflect a general correlation between adsorption energy and the shift of E_d. In this case, the improvement of the intrinsic activity as well as the optimization of the interaction with oxygen-containing intermediates can be further facilitated by modulating d-band electronic structures of transition metal atoms. Doping with heteroatoms [23], constructing hetero-interfaces [24], and regulating the Fe-spin state [2,25] are generally applied to realize electron modulation. When compared to mono-atom catalysts, dual-atom catalysts have essentially different coordination environments and identified two key types of active sites (Co_2/Fe-N_{10} and Fe-N_4/Ni-N_4) [26,27]. Meanwhile, strong electronic coupling occurs between the double atomic pairs, enhancing the d-electron density near the Fermi energy level and synergistically accelerating the adsorption

* Corresponding authors at: School of Metallurgy and Environment, Central South University, Changsha 410083, China.
E-mail addresses: tianzhongliang@csu.edu.cn (Z. Tian), laiyanqing@csu.edu.cn (Y. Lai), g.he@ucl.ac.uk (G. He).

https://doi.org/10.1016/j.ensm.2023.04.003
Received 12 December 2022; Received in revised form 18 March 2023; Accepted 3 April 2023
Available online 5 April 2023

and dissociation of the intermediates [28]. It is well-known that the performance of an atomic catalyst depends not only on its intrinsic activity, but also on the density and distribution of the exposed active sites [29]. Therefore, synthesizing precisely controllable and highly dispersed diatomic catalysts is still challenging. A deeper understanding of the catalytic process in terms of interactions and kinetic pathways on the microscopic interfacial layers is equally crucial [30].

Herein, we developed a curved nitrogen-doped hollow carbon diatomic catalyst (Fe/Zn-CNHC) that achieved excellent electrocatalytic stability while maintaining a high intrinsic activity. The introduction of Fe/Zn atoms is based on the protonated use of nitrogen-doped carbon substrates with moderate coordination strength to the metal during the confinement heat treatment, resulting in the equilibrium dispersion of the atoms on the substrate. Meanwhile, surfactants boost to regulate the micro-interfacial environment of the ZIF-8 and enhance the stability of the catalyst structure. In addition, the unique coordination structure, revealed by extended X-ray absorption fine structure (EXAFS) and density functional theory (DFT), leads to the left shift of Fe 3d orbitals from projected d-density of states (PDOS) and approaching to E_d, which optimizes the binding of the ORR intermediates. Benefiting from these features, Fe/Zn-CNHC shows reinforced ORR activity, overwhelming the 20% Pt/C benchmark. This work opens a new avenue to improve the ORR performance of transition metal-based catalysts, and inspires electronic localization of active sites for regulating catalytic activity.

2. Experiment

2.1. Chemicals

Iron acetylacetone ($Fe(acac)_3$, AR), zinc nitrate ($Zn(NO_3)_2{\cdot}6H_2O$, AR), 2-methylimidazole (2-MeIM, AR), polyethylene oxide–polypropylene oxide–polyethylene oxide (P123, AR), potassium hydroxide (KOH, AR), methanol (CH_3OH, ~ 98 wt.%), Melamine ($C_3H_6N_6$, AR), anhydrous ethanol (AR), Pt/C (20 wt.% Pt on Vulcan XC-72R) were purchased from Sigma-Aldrich and used as received without further purification.

2.2. Catalyst synthesis

Synthesis of ZIF-8@P123 precursors: $Zn(NO_3)_2{\cdot}6H_2O$ (1.16 g), P123 (0.2 g), and 2-MeIM (1.32 g) were generally dissolved in 45 ml methanol for the production of ZIF-8@P123. Under stirring, equal volumes of the two solutions were combined. After a few minutes, a milky tint developed, indicating that coordination bonds between Zn^{2+} sites and N in 2-MeIM ligands had formed. The as-obtained ZIF-8 product was recovered by filtration after 12 hours of additional reaction at room temperature, twice washed with methanol, and lastly dried at 65°C for 8 hours.

Synthesis of Zn-CNHC and Fe/Zn-CHNC catalyst: 200 mg of ZIF-8@P123 precursor was disseminated in 50 ml methanol, and then 50 ml of 0.014 M $Fe(acac)_3$ methanol solution was added into the ZIF-8 solution above. The aforesaid combination solution was injected with 20 ml of methanol containing 0.462 g 2-MeIM and stirred continuously overnight at room temperature. Then, 0.418 g $Zn(NO_3)_6.H_2O$ dissolved in 20 ml methanol was added. Finally, the Fe/ZIF-8@P123 was collected by centrifugation at 10500 rpm for 3 minutes and rinsed numerous times with methanol. Fe/ZIF-8@P123 powder was obtained after drying the solid at 65°C in vacuum for 8 hours. The as-prepared Fe/ZIF-8@P123 and ZIF-8@P123 were mixed with an equal amount of melamine and then thermally maintained at 900 and 1100°C for 3 hours under flowing Ar atmosphere at a ramp rate of 5°C min^{-1} in muffle furnace. Zn-CNHC and Fe/Zn-CNHC were collected correspondingly and without any treatment after cooling to room temperature naturally.

Synthesis of Fe-CNHC catalyst: The as-prepared Fe/ZIF-8@P123 was thermally maintained at 900°C for 3 h under flowing Ar atmosphere at a ramp rate of 5°C min^{-1} in tube furnace (120 ml/min).

2.3. Materials characterization

The surface morphology of as-prepared catalysts were studied by scanning electron microscope (SEM, TESCA NMIRA3 LMU, CSU, USA). Transmission electron microscopy (TEM, Tecnai G2 F20 S-TWIN TMP, CSU, USA) were used to investigate the microstructures of catalysts. The elementary composition of the catalysts was characterized by Oxford energy-dispersive X-ray spectrometer (EDX), which is attached to TEM equipment. The phase composition of the as-prepared catalysts were tested by X-ray diffraction (XRD, Empyrean, Malvern Panalytical., Shiyanjia Lab, Netherlands) with Cu Kα radiation (λ=1.5406 Å). The X-ray photoelectron spectroscopy (XPS, Thermo Scientific K-Alpha, Thermo Fisher Scientific, Shiyanjia Lab, USA) was analyzed on K-Alpha$^+$ system, and calibrated by C 1s (284.8 eV). The X-ray absorption spectroscopy were recorded on Beamline TPL14A1 of Taiwan light source at National Synchrotron Radiation Research Center (NSRRC). The content of Zn and Fe in Fe/Zn-CNHC catalysts were measured by inductively coupled plasma optical emission spectrometer (ICP-OES, Agilent 720ES, Shiyanjia Lab, USA). The gas chromatography (GC-2014C, Shimadzu, BUCT, Japan) was employed to detect H_2 quantification and the carrier gas is ultrapure argon (Ar, 99.999%). Raman (Thermo Scientific DXR2, HNU, USA) spectra were obtained using a DXR2 Raman Microscope with a wavelength of 532 nm. The isolated Zn-Fe atom pair were observed through high-angle annular dark-field scanning transmission electron microscope (HAADF-STEM) with a spherical aberration corrector. X-ray absorption find structure (XAFS) was detected at the BL14W1 in Shanghai Synchrotron Radiation Facility (SSRF). The extended X-ray absorption fine structure (EXAFS) data were analyzed using Athena software.

2.4. Electrochemical measurements

At room temperature, electrochemical measurements of catalysts were performed using a Gamry Interface 1000 electrochemical workstation equipped with a standard three-electrode system. Dropping the catalyst ink onto a glass-carbon (GC), which is a rotating disk electrode (RDE, 5 mm in diameter). The catalyst ink was made by dispersing 5 mg of each catalyst in 1 mL of a mixed solution including 0.98 mL of ethanol/water (1:1, v/v) and 20 mL of 5% Nafion solution, then ultrasonication for 30 minutes to make a homogeneous black suspension solution. The catalyst ink was then dropped onto the surface of the GC electrode and allowed to dry in the air. The catalyst loading amount was 0.3 mg cm^{-2} for both as-prepared catalysts and commercial Pt/C (20 wt %).

The catalysts' ORR performance was tested in an O_2-saturated 0.1 M KOH solution. At a scan rate of 50 mV s^{-1}, the cyclic voltammetry (CV) curves were obtained. RDE was used to perform linear sweep voltammetry (LSV) at a scan rate of 5 mV s^{-1} with varying rotation speeds (400, 625, 900, 1225, 1600, and 2025 rpm). The standard reversible hydrogen electrode is used to compare all measured potentials (RHE). The onset potential was defined as the potential required for generating a current density of -0.1 mA cm^{-2} in LSV curves. The electron transfer number was calculated by Koutecky-Levich (K-L) equation:

$$\frac{1}{J} = \frac{1}{J_K} + \frac{1}{J_L} = \frac{1}{J_K} + \frac{1}{B\omega^{1/2}} \quad (1)$$

$$B = 0.62nFC_0D_0^{\ 2/3}\upsilon^{-1/6} \quad (2)$$

where J_k is the kinetic diffusion current density, JL is the kinetic limiting current density, B is the reciprocal of the slope, is the angular velocity (=2N, N is the rotation speed), n is the transferred electron number, F is the Faraday constant (96485 C mol^{-1}), C0 is the saturated concentration of O_2 (1.210^{-6} mol cm^{-3}), D0 is the diffusion coefficient of O_2 (1.910^{-5} cm^2 s^{-1}), and v is the (0.01 cm^2 s^{-1}).

Accelerated degradation tests (ADT) at a scan rate of 100 mV s^{-1} for

5,000 cycles between 0.2 and 1.1 V were used to assess the ORR stability of the electrocatalysts in the O_2-staurated 0.1 M KOH solution (vs. RHE). Chronoamperometry was used to test the electrocatalysts' ORR stability in O_2-staurated 0.1 M KOH at a potential of 0.70 V (vs. RHE). LSV was done using RDE at a scan rate of 5 mV s^{-1} to test tolerance to KSCN.

Assembly of Al-air batteries: The polished aluminum plate serves as the anode in most Al–air batteries. In a home-made cell model, the electrolyte is 6M KOH containing 0.0005 M $In(OH)_3$, 0.0075 M ZnO, and 0.01 M Na_2SnO_3; the cathode is a gas diffusion electrode with a catalyst loading amount of 2.0 mg cm^2. The commercial Pt/C was likewise built in a similar manner as a control. The LAND testing system was used to perform battery measurements.

2.5. Theoretical calculations

Vienna Abinitio Simulation Package was used to undertake the theoretical study based on density function theory (DFT) computations (VASP). The electron-valence energy was described using the projector augmented wave (PAW) approach and the generalized gradient approximation (GGA) using a Perdew-Burke-Ernzerhof (PBE) functional. For the plane-wave basis set, an energy cutoff of 500 eV was employed. The energy and force convergence thresholds were established at 10^{-5} eV and 0.02 eV/, respectively. The vacuum layer thickness was set to 20 to prevent interaction between two neighboring images. To account for dispersion interactions, a semi-empirical van der Waals (vdW) correction developed by Grimme (DFT-D3) was used.

The free energy of each elementary step in the proton coupled electron transfer reactions was computed using the computational hydrogen electrode (CHE) model for oxygen reduction reaction (ORR). Considering the O_2 molecular is not broken before reduction, the associative $4e^-$ reduction pathway was evaluated to be most feasible for ORR in this work, as follows:

$$O_2 + * \rightarrow O_2 * \quad (3)$$

$$O_2 * + H_2O + e^- \rightarrow OOH^* \quad (4)$$

$$OOH^* + e^- \rightarrow O^* + OH^- \quad (5)$$

$$O^* + H_2O + e^- \rightarrow OH^* + OH^- \quad (6)$$

$$OH^* + e^- \rightarrow OH^- + * \quad (7)$$

where * represents the active site on the corresponding surface.

3. Results and discussion

3.1. Catalyst characterization

The electronic structure of an ORR electrocatalyst is known to be intrinsically linked to the adsorption energy of reaction intermediates. Before synthesizing the Fe/Zn-CNHC electrocatalysts, PDOS were carried out to evaluate the charge distribution of these Fe active sites (Fig. 1a). Clearly, the E_d energy level of Fe/Zn-CNHC is higher than that of Fe-CNHC, suggesting that the E_d energy levels are closer to the Fermi level (E_F) after introducing Zn. The construction mechanism of the Fe/Zn-CNHC phase-junction electrocatalyst is shown in Fig. 1b. The selective cleavage of the Zn induces the incorporation of the electron-withdrawing status on the active center of FeN_4, thus forming a unique electronic structure. Especially, the electronic interaction can be seen as a coupling between the valence state of the adsorbate and the D state of the transition metal, leading to the creation of split bonds and the upward shift of E_d, which is beneficial for the adsorption of O_2 for accelerating the proton-coupled electron transfer processes [25], thus accelerating entire ORR process.

As illustrated in Fig. 2a, a series of Fe/Zn-CNHC catalysts were fabricated via a facile two-step procedure (the detailed process is displayed in the experiment section). Firstly, Fe-doped ZIF-8@P123 (Fe/ZIF-8@P123) precursors were prepared by precisely controlling Fe doping amount in a simple polymerization process. Subsequently, the as-obtained Fe/ZIF-8@P123 precursors were carbonized using a thermal reaction to synthesize the X-Fe/Zn-CNHC (X stands for temperature) catalysts in the muffle furnace under argon atmosphere with ZIF-8 as both carbon and nitrogen sources (Fig. S1). ZIF-8 forms a continuous carbon frame after thermal reaction, which can not only provide a multi-dimensional electron transfer pathway but also improve the electrical conductivity of the catalysts [31]. To further analyze the formation mechanism of the Fe/Zn-CNHC hollow structure, we conducted a series of temperature-controlled experiments. We investigated the effect of the temperature, and tracked the evolutionary trajectory of hollow

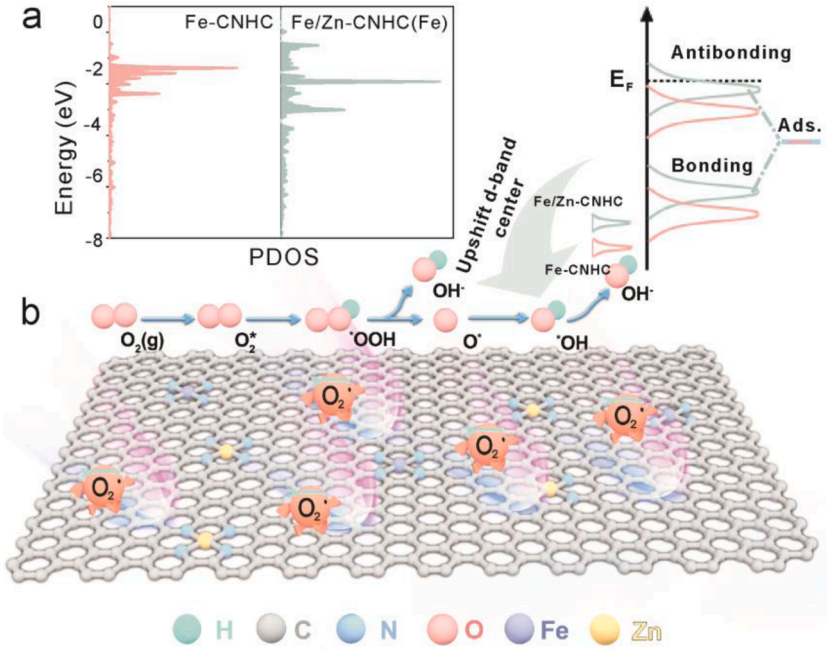

Fig. 1. Design of the Fe/Zn-CNHC catalyst: (a) PDOS of Fe for Fe-CNHC and Fe/Zn-CNHC; (b) Reaction pathway of the Fe/Zn-CNHC catalyst.

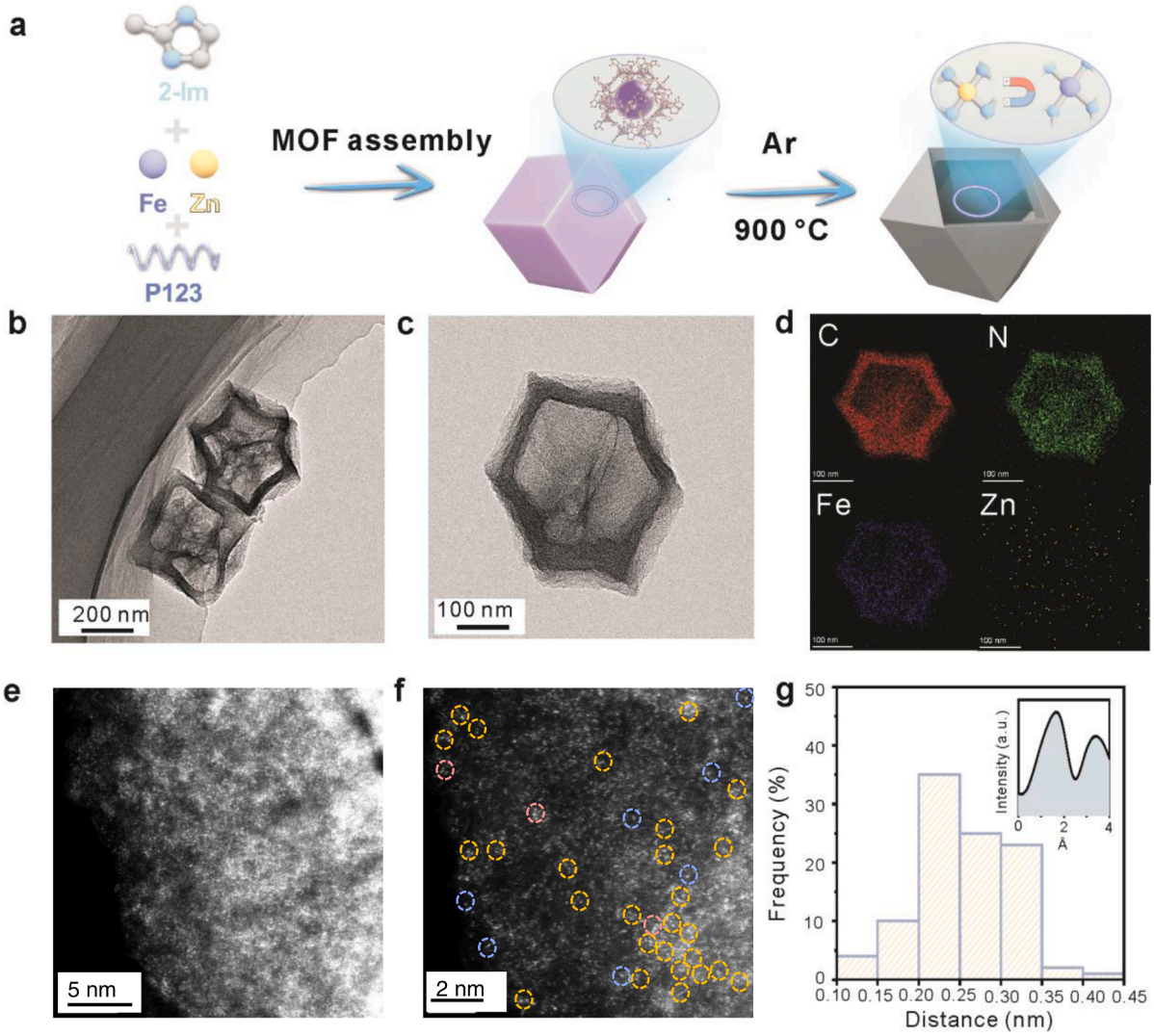

Fig. 2. The microstructure characterization. (a) Schematic illustration for the synthesis process of Fe/Zn-CNHC catalyst; (b, c and d) TEM image and EDS element maps (Fe: orange, C: red, N: green, Zn: yellow) of Fe/Zn-CNHC at the pyrolysis temperature of 900°C; (e and f) AC HAADF-STEM images of Fe/Zn-CNHC; (g) Statistical Fe/Zn distance in the observed diatomic pairs. Inset is the intensity profile obtained on bimetallic Fe/Zn sites.

structures at 500, 900, and 1100°C, as schematically illustrated in Fig. 2b,c and Fig. S2. The results of scanning electron microscopy (SEM) and transmission electron microscopy (TEM) were used to analyze the overall morphology of the prepared catalysts. (Fig. S3) Typical Fe/Zn-CNHC materials with Fe atoms exposed on the surface of the dodecahedron were produced via pyrolysis of ZIF-8@P123 under Ar at 900°C. In contrast to the standard ZIF-8 synthetic technique, P123 was added to the new system's initial precursor solution as adjusting the favorable aperture.

The planar surfaces of Fe/ZIF-8@P123 are partially etched at 500°C pyrolysis temperature, while the pristine structure is preserved. Within the framework, the crystal surface is rather smooth, with dominating micropores connected with 3D hydrocarbon networks. The surface and internal regions of ZIF-8@p123 were further removed by pyrolysis at 900°C, resulting in a curved framework structure with a hollow interior and interconnected edges. This unique structure results in a concave morphology with rough and shrinking surfaces, which differs from ZIF-8 Which is commonly obtained. During the development of hollow structures, the framework offers support to avoid the collapse and fracture of shell layers. The facets of matching carbon particles become less distinct, and the particles become more porous, with many micropores on the surfaces (up to 2 nm). Active areas are thought to lie inside or near the micropores of carbon supports, according to research [32, 33]. The related TEM images and EDS mappings in various stages are displayed in Fig. 2d to depict the morphology and distribution of elements, which significantly confirms the preceding findings. The Kirkendall effect is followed in this method [34]. The surfactant P123 and Zn^{2+} ions undergo continuous unequal interdiffusion at the core and shell interfaces of the dodecahedron, which leads to the appearance of Kirkendall voids. As the Kirkendall effect process proceeds, the internal ZIF-8 gradually decomposes and forms a uniformly thick hollow structure. The presence of P123 can also further guide the tendency of the shell framework to be curved. When the pyrolysis temperature continues to rise and is maintained at 900°C for 3 hours, most of the residual zinc in the shell is removed in the form of vapor, thus building the desired complete hollow structure. Then, under the thermal treatment at 1100°C, the size and shape of ZIF-8 crystals are difficult to maintain efficiency in catalysts. The polyhedral carbon particles become blurred and even partially broken in the catalyst.

The metals were atomically distributed, as demonstrated by aberration-corrected high-angle annular dark-field scanning transmission electron microscopy (HAADF-STEM). There were numerous, uniformly spaced, isolated bright spots on the carbon matrix, and no metal nanoparticles had formed (Fig. 2e). Many metal-pair locations can

be seen more clearly by expanding the magnification of the atomic-resolution HAADF-STEM image (Fig. 2f). For accuracy, different forms of atoms are marked with different colored circles. Most of them are in the form of diatomic pairs, with only a small number of single or poly-atomic configurations. The electron energy loss spectrum (EELS) (Fig. S4) reals the coexistence of Fe and Zn elements in Fe/Zn-CNHC. Based on the observation of more than 100 atomic pairs with a distance of about 0.25 nm between two bright points, the formation of a double atomic pair is demonstrated. Other individual bright dots marked by blue circles are identified as isolated Fe or Zn single atoms, indicating that the Fe/Zn atomic pair, single Fe and Zn atoms, coexisted on the CNHC. According to the EDS, it was shown that the elemental distribution of Fe, Zn, N, and C is homogeneous in the whole framework (Fig. S5). SEM images and X-ray diffraction (XRD) patterns confirm that the morphology and structures of ZIF-8 remain unchanged after the introduction of P123 (Fig. S6). The XRD peaks of Fe/Zn-ZIF@P123 are consistent with that of ZIF-8@P123 without any impurities. Meanwhile, Fe/Zn-CNHC catalysts show two broad peaks at 25.2 and 43.7°, assigning to the (002) and (101) crystal planes of carbon, respectively (Fig. S7) [35]. Notably, no diffraction peak ascribed to metallic Fe or other Fe-based species can be detected, indicative of the atomically dispersed Fe single atoms in the Fe/Zn-CNHC. Meanwhile, high-resolution transmission electron microscope (HRTEM) confirmed the phenomenon that only disordered amorphous carbon exists (Fig. S8).

BET surface areas of Fe/Zn-CNHC, Zn-CNHC, and Fe-CNHC are 1351, 835, and 796 $m^2\ g^{-1}$, respectively, based on N_2 sorption isotherms. Due to the addition of P123, the produced catalysts had a wider micro-pore size distribution (Fig. S9). Meanwhile, the interaction of different metals also affects the morphology of the catalyst. Through inductively coupled plasma mass spectrometry (ICP), the Fe and Zn loading are 0.98 *wt*% and 2.87 *wt*%, respectively. Additionally, the metal contents of the other catalysts are shown in Table S1. The overall N doping determined by XPS is summarized in Fig. 3a. The four types of N species found in all catalysts are pyridinic N (398.5 eV), pyrrolic N (399.5 eV), graphitic N (400.7 eV), and oxidized N (402.7eV) [36]. Through Zn capture, the total content of pyridinic N and pyrrolic N increases in the Fe/Zn-CNHC catalyst (Fig. 3b). Meanwhile, based on the previous reports, pyridinic N can not only operate as active sites for ORR activity, but it can also create Fe/Zn-CNHC moieties by covalently coordinating with the neighboring metal atoms [15,16]. Changing the gas partial pressure environment at high temperatures affects the metal-nitrogen content, but the nitrogen content is not the key factor affecting the activity. The four types of C species found in all catalysts are C=O, C-O, C-N, and C-C group (Fig. S10). Carbon-oxygen species are regarded as defects that facilitate ORR in alkaline media. sp^2 C also improves ORR activity due to its high electrical conductivity. Furthermore, due to the little amount of Fe in each catalyst, the Fe 2p signal could not be identified in all of them, as shown in Figs. S11 and S12 [19]. This is consistent with the ICP results.

X-ray absorption near edge structure (XANES) and X-ray absorption fine structure (EXAFS) spectra were used to identify precise electronic structures and local coordination environments of the Fe/Zn-CNHC. We carried out EXAFS characterization to verify the atomic dispersion of Fe species and their coordination structure. According to the energy of the absorption edge, the oxidation state of the Fe atoms in Fe/Zn-CNHC is near +3 (Fig. 3d). Moreover, the pre-edge peak of Fe/Zn-CNHC located

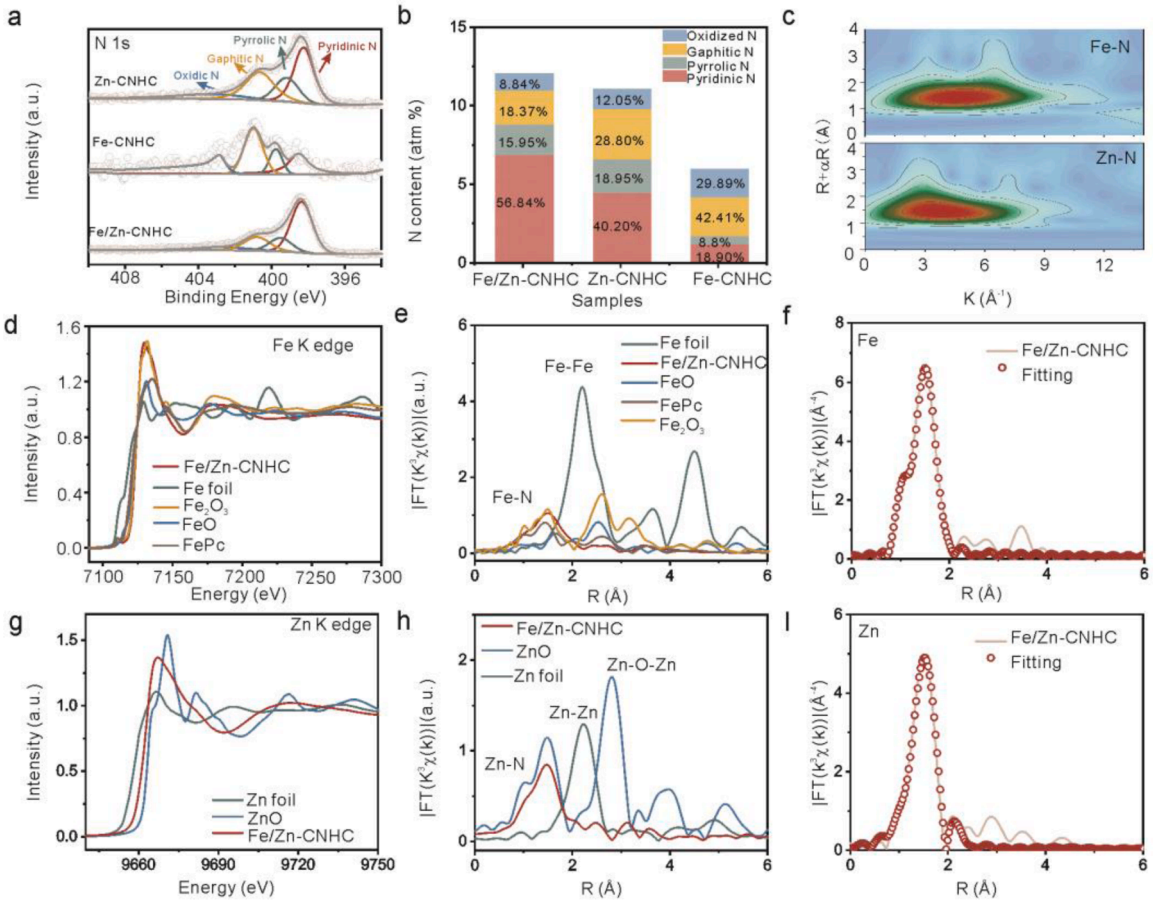

Fig. 3. Structural characterization of the Fe/Zn-CNHC catalysts. (a) XPS N 1s spectra; (b) fraction of various types of nitrogen; Wavelet transform contour plots of (c) Fe-N_4 and Zn-N_4; (d) Fe K-edge XANES and (e) Fourier-transform EXAFS spectra; (f) Corresponding EXAFS fitting curves at the Fe K-edge of Fe/Zn-CNHC; g) Zn K-edge XANES and h) Fourier-transform EXAFS spectra; i) Corresponding EXAFS fitting curves at the Zn K-edge of Fe/Zn-CNHC.

at 7113 eV is very close to that of Fe_2O_3, further confirming the +3 valence state of the Fe atoms in Fe/Zn-CNHC [37]. From the *R* space of Fe/Zn-CNHC catalyst, only a Fe-N peak at 2.36 Å is observed, confirming its atomic dispersion [38]. The subsequent least-squares EXAFS fit analysis demonstrated that the Fe atomic site was coordinated to four N atoms and the bond length of Fe to N was 2.02 Å (Fig. 3e,f and Table S2). Fig. 3g–i show electronic structures and local coordination environments of the Zn atoms in Fe/Zn-CNHC. Based on the observation that the position of the absorption edge of zinc in the K-edge XANES spectrum is between that of the Zn foil and ZnO, its valence state was shown to be between 0 and +2. The peak at 1.5 Å is assigned to the scattering path of Zn-N. The Zn-Zn and Zn-O-Zn bonds are not monitored. The fitted coordination number between the Zn atom and N is 4, and its bond length is 2.03 Å (Fig. 3i and Table S2), respectively. Therefore, we suggest that the Fe/Zn diatomic sites are homogeneous in the form of atomically dispersed FeN_4 and ZnN_4 structures. Fig. S14 shows the k-space spatial oscillations of Fe and Zn atoms, respectively, which provide data support for the fitting of the coordination numbers and bond lengths of the above-mentioned coordination metal atoms, and the R-space data can be extracted by Fourier transform. Plots of R and K spatial energy oscillations of Fe and Zn foils as comparison are presented in Fig. S13. The wavelet transform (WT) analysis of the EXAFS oscillations of Fe/Zn-CNHC was performed to visualize the dispersion of metal atomic sites at radial distances and K-space in high-resolution maps (Fig. 3c). These results further confirm that the atomic dispersion of the Fe and Zn sites with M-N_4 conformation are well-established.

2.2. Electrocatalytic Oxygen Reduction Performance

The ORR activities of the three prepared catalysts (Fe/Zn-CNHC, Fe-CNHC, and Zn-CNHC) were first tested in O_2-saturated 0.1 M KOH solutions and compared using 20% Pt/C catalysts. All potentials in the graphs are converted relative to the reversible hydrogen electrode (vs. RHE). Fig. 4a shows that Fe/Zn-CNHC has the highest positive $E_{1/2}$ (0.91 V) of all manufactured catalysts, outperforming commercially available 20% Pt/C ($E_{1/2}$, 0.86 V), Fe-CNHC ($E_{1/2}$, 0.88 V), Zn-CNHC ($E_{1/2}$, 0.79 V), and non-precious metal atomic catalysts in general (Table S3). In comparison to Pt/C (2.36 mA cm^{-2}), Fe-CNHC (4.21 mA cm^{-2}), and Zn-CNHC (0.83 mA cm^{-2}), Fe/Zn-CNHC likewise produces the highest kinetic current density (J_k) of 7.45 mA cm^{-2} at 0.90 V (Fig. 4b). A smaller Tafel slop of Fe/Zn-CNHC (67.7 mV dec^{-1}) compared with that of Pt/C (76.4 mV dec^{-1}), Fe-CNHC (76.4 mV dec^{-1}), and Zn-CNHC (224.5 mV dec^{-1}) further confirmed its superior ORR kinetics (Fig. 4c). From cyclic voltammetry (CV) curves (Fig. S15), Fe/Zn-CNHC displays a well-defined cathodic peak at 0.91 V, implying the significant role of Fe/Zn-CNHC in boosting ORR kinetics. The LSV of the 20% Pt/C, Fe/Zn-CNHC, Fe-CNHC, and Zn-CNHC electrocatalysts were then tested in 0.1 M $HClO_4$. The $E_{1/2}$ of the ORR on the Fe/Zn-CNHC is huge in 0.1 M $HClO_4$ (Fig. S16), indicating its inferior ORR activity. The corresponding Tafel slope of the Fe/Zn-CNHC electrocatalyst is 102.1 mV dec^{-1} in 0.1 M $HClO_4$, much smaller than that of the Fe-CNHC electrocatalyst (107.1 mV dec^{-1}) and that (156.9 mV dec^{-1}) of the Zn-CNHC electrocatalyst. The rotating disk electron transfer numbers at various rotation rates were carried out to assess the ORR pathway of Fe/Zn-CNHC (Fig. 4d). The Fe/Zn-CNHC catalyst was tested for LSV at 400–2500 rpm and the Koutecky-Levich curve obtained, by calculating its electron transfer number between 3.98 and 4.03, was greater than the other prepared catalysts and 20% of the 20% Pt/C catalyst (Fig. S17), indicating a perfect four-electron ORR pathway [39]. The electrochemically active specific surface area (ECSA) is obtained by measuring the double-layer capacitance (C_{dl}) of the catalyst, which can be used as a powerful parameter related to the catalytic properties of the catalyst surface. Fe/Zn-CNHC shows the highest C_{dl} of 4.63 mF cm^{-2} and the largest ECSA of 115.75 m^2 g^{-1} compare to Fe-CNHC (1.86 mF cm^{-2} /46.5 m^2 g^{-1}) and Zn-CNHC (1.42 mF cm^{-2} / 35.5 m^2 g^{-1}) (Fig. S18 and S19). In addition, to exclude the contribution of ECSA to the ORR performance, all samples of j_k from the measured were subjected to ECSA normalization. j_k curves normalized by ECSA showed the same trend as the corresponding LSV curves (Fig. S20), again indicating the outstanding ORR intrinsic activity of Fe/Zn-CNHC [40]. Moreover, the kinetic current density was normalized by loading the mass of catalyst to give the kinetic mass specific activity (j_m) [41,42]. As shown in Fig. S21, the j_m of Fe/Zn-CNHC is determined to be 36.52 A g^{-1}, which is 1.8 and 9.1 times higher than those of Fe-CNHC and Zn-CNHC, respectively. This result suggests that the utilization of active sites for Fe/Zn-CNHC is much higher under the same mass loading, further demonstrating the

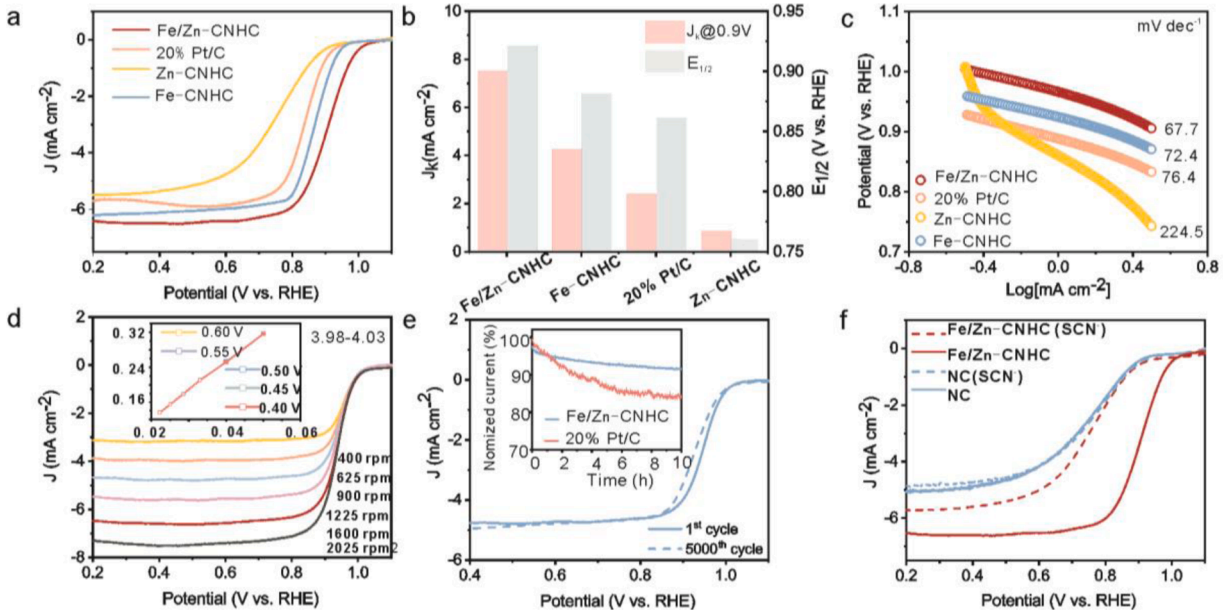

Fig. 4. ORR activity and durability evaluations. a) LSV curves of Zn-CNHC, Fe-CNHC, Fe/Zn-CNHC, and 20% Pt/C in O_2-staurated 0.1 M KOH solution at 1600 rpm; b) J_k at 0.90 V and $E_{1/2}$ for these catalysts; c) Tafel slopes for Fe/Zn-CNHC and Pt/C; d) LSV curves of Fe/Zn-CNHC at different rotating rates (inset: K-L plots); e) LSV curves of Fe/Zn-CNHC before and after 5,000 cycles (inset: Normalized chronoamperometry curves of Fe/Zn-CNHC and 20% Pt/C at the constant potential of 0.7 V vs. RHE); f) effect of SCN^- interaction on the catalytic activity of Fe/Zn-CNHC and NC.

introduction of ZnN_4 can facilitate the intrinsic activity and boost ORR kinetics. To understand the origin of the observed high durability of the Fe/Zn-CNHC catalyst, we carried out XPS measurements to monitor changes for Fe/Zn-CNHC electrocatalysts before and after accelerated stress tests (Figure S23-25). The high-resolution Zn 2p spectrum exhibits two main peaks at 1021.4 eV (2p3/2) and 1044.6 eV (2p1/2), attributing to the oxidation state of Zn single atom. Notably, the Zn species have no significant change during the ex-situ test, except for the slightly positive shift. It can be ascribed to the electron transfer from Zn to Fe during the reaction, as well as the adsorption of oxygen containing intermediates [43]. Beyond that, the Fe/Zn-CNHC catalyst exhibited a relatively small decrease in pyridinic-N content from 56.8% to (32.6–52.6) % after accelerated stress tests. In general, Fe/Zn-CNHC catalysts largely retained their ZnN_4 and FeN_4 active sites after the long-term operation. The performance of the long-term stability of Fe/Zn-CNHC was effectively evaluated by high-speed cyclic voltammetry tests. After 5,000 CV cycles, the LSV curve showed no significant attenuation and a negative shift of only 7mV (Fig. 4e). The outstanding stability is also confirmed by chronoamperometry. After 10 hours at 0.7 V vs. RHE in an O_2-saturated electrolyte, Fe/Zn-CNHC can maintain 93.2% of the initial current density. However, under the identical conditions, commercial Pt/C maintained 85.6% retention. At the same time, to further demonstrate the Zn-Fe atomic pair as the real active site, the introduction of SCN^- in the test system resulted in a significant negative shift of 130 mV in the half-wave potential, a significant decrease in the diffusion-limited current density (=85% retention), and a significant poisoning of the metal atoms, while no significant changes were found in the prepared porous NC, indicating that the Fe-N_4 site constitutes the key active center of the ORR (Fig. 4f).

The effect of Zn-load amounts on the ORR activity of Fe/Zn-CNHC catalysts are also investigated. As shown in **Fig. S26**, When the atom % Zn is ca.2.87, the Fe/Zn-CNHC shows the highest positive $E_{1/2}$ and lowest activity. Both the lower and higher amounts of Zn-load will decrease its ORR activities. The reason may be that the E_d energy levels of Fe are tailored by the Zn-load amounts, which is closely linked with the adsorption and desorption capabilities for the ORR intermediates.

2.3. DFT calculations

With the information of the composition and structure of Fe/Zn-CNHC active sites, the DFT calculation was conducted to explore the detailed electronic and geometric structures of the active sites for ORR. Fig. S27 reveals the optimized geometric model of simulated Zn-CNHC, Fe-CNHC and Fe/Zn-CNHC electrocatalysts. The electron charge density distribution shows that the non-uniform charge distributions are intensified after introducing Zn. Fig. 5a-c shows that the electron density of Fe centered structures in Fe/Zn-CNHC is higher than that of Fe-CNHC. In comparison to Zn-CNHC, Fe/Zn-CNHC has a lower electron density. In the Fe-CNHC and Zn-CNHC model, the charge numbers of Fe and Zn sites were 1.06 eV and 1.35, respectively, while this value is promoted to 1.43 eV of the Fe/Zn-CNHC, revealing a valence state transition from Fe^{3+} ($3d^5$) to Fe^{2+} ($3d^6$) [26,44]. Additionally, DOS was employed to estimate the binding strength among the metal center and non-metal atoms (C and N) [45]. As illustrated in Fig. 5d–f, an obvious energy negative shift for O_2 adsorption of single-metal atom center (Fe-N_4: -1.90eV, Zn-N_4: -1.61eV) can be observed on the dual-metal atom centered structures (-2.10 eV). Interestingly, the bimetal structure loses more electrons while C gains more electrons, which is consistent with the DOS results (Fig. S28). Based on previous reports, the introduction of Zn spontaneously causes the generation of spin-polarized electrons at the Fermi energy level. More specifically, the 3d band is intrinsically narrow for Fe-CNHC and broadened when combined with Zn, illustrating an upshift of E_d [28,46]. Based on the PDOS analyses (Fig. S29) and d-band theory, an upshift of the d-band center for the electrocatalysts (Fig. 5g) is attributed to the charge transfer between the metal sites. The d-band of Fe/Zn-CNHC shifts close to Fermi level, and enhances the capture of the O_2 molecule that is the initial step of ORR [47].

ORR processes on different sites were estimated at 1.23 V and

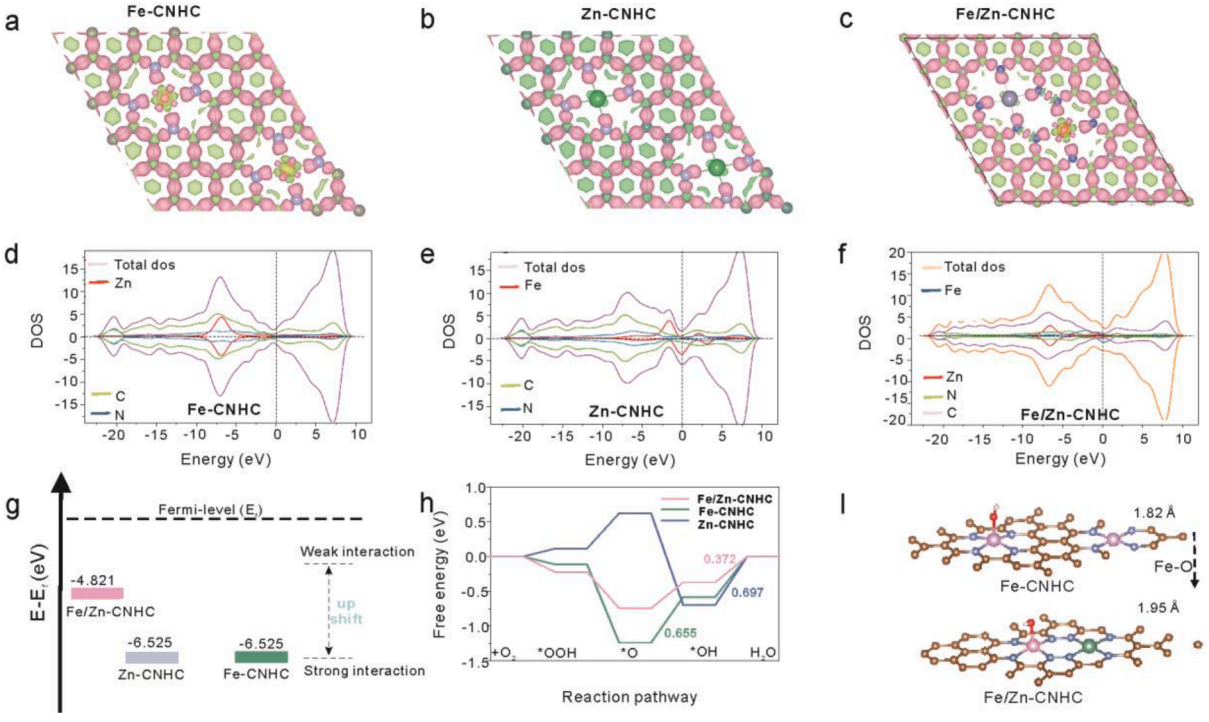

Fig. 5. Calculated charge density differences for (a) Fe-CNHC, (b) Zn-CNHC and (c) Fe/Zn-CNHC (red and green areas, respectively represent charge density increase and decrease; larger values represent increased electron density); The DOS of (d) Zn-CNHC, (e) Fe-CNHC and (f) Fe/Zn-CNHC catalysts; (g) the schematic of d-band center distance from Fermi-level to decrease O_2-metal interaction; (h) Free energy diagram for the ORR process on three models at the equilibrium potentials of U=1.23 V; (i) ΔG_{*OH} and the metal-O bond length variation for Fe-CNHC and Fe/Zn-CNHC.

compared to further confirm the electrocatalytic active center, as shown in Fig. 5h. The electron density of Fe-CNHC decreases by 0.11 eV after O_2 adsorption, while Fe/Zn-CNHC increases by 0.19 eV. It is further proved that the existence of Zn can increase the electronegativity of Fe centers structures in Fe/Zn-CNHC, which is conducive to the adsorption of intermediates and the breakage of O-O bonds. The presence of Zn can effectively increase the electronegativity of the Fe central structure in Fe/Zn-CNHC, thus facilitating the adsorption of intermediates and the dissociation of O-O bonds [48,49]. At each step of the ORR reaction pathway, the difference in adsorption energy between reactants and products was calculated. Given that the d-band center of Fe-Zn/CNHC is in a more favorable position, O_2 molecules are more favorably adsorbed on their active sites, accelerating the subsequent O-O breakage. For OOH*, O* and OH* oxygen-containing intermediates adsorbed on the Zn site of Zn-CNHC, the Fe site of Fe-CNHC and the Fe site on Fe/Zn-CNHC, the OH* intermediates show the highest adsorption energies, indicating that the determining steps of the ORR are the formation and decomposition of the OH* intermediates. Among them, the adsorption energy of Fe-Zn/CNHC is the lowest compared to Fe-CNHC and Zn-CNHC, which is also consistent with the results of electrochemical properties [48]. The Fe-O bond length increases in Fe/Zn-CNHC for the *OH reaction intermediate, i.e. Fe-O increases from 1.82 to 1.95 Å (Fig. 5i), which is in good agreement with the fact that G_{*OH} decreases in Fe/Zn-CNHC. Fe/Zn-CNHC has the smallest energy difference among the O* and OH* intermediates, indicating good ORR activity. Furthermore, when compared to Fe-CNHC (0.655 eV) and Zn-CNHC (0.697 eV), the formation energy of intermediates on Fe/Zn-CNHC (0.372 eV) is much lower. However, when the distance between Fe and Zn atoms exceeded 5 Å, the adsorption potential of oxygen-containing intermediates increased, which is in agreement with the HAADF-STEM results that the Zn-Fe atom pair at the appropriate distance is favorable for ORR activity (Fig. S30).

2.4. Aluminum-air battery performance

In addition, the performance of the air cathode prepared from Fe/Zn-CHNC catalyst was evaluated in the flow cell system depicted in Fig. 6a, using 20% Pt/C as a comparison [50,51]. The designed flow cell consists of an aluminum anode, an electrolyte, and an air cathode [52]. As expected, the power density of the Fe/Zn-CNHC anode (100 mW cm^{-2}) was substantially higher compared to Pt/C (80 mW cm^{-2}) (Fig. 6b). Then, we evaluated the discharge performance of the catalyst at different discharge current densities (Fig. 6c). It is clear that Fe/Zn-CNHC exhibits better rate capability and fast dynamic response compared to Pt/C. The open circuit potentials of Zn/Fe-CNHC and Pt/C are -1.80 and -1.75 V, respectively. Fe/Zn-CNHC also exhibits superior operating voltage for high current density operation. The discharge curves shown in Fig. 6d indicate that the Al-air cell assembled with Fe/Zn-CNHC can provide a specific capacity of 856 mAh g^{-1} at a high current density of 100 mA cm^{-2}, which is greater than that of the cell assembled with Pt/C (782 mAh g^{-1}). Its stability as an air positive electrode was further evaluated with excellent cycling stability (100 h) at a current density of 25 mA cm^{-2}. After 100 h of operation, the voltage gap decreased by only 0.06 V, with an extremely low decay rate of 0.01% per hour (Fig. 6e).

4. Conclusion

In summary, a novel mechanism with the introduction of atomic Zn into Fe-N_4 coordination is unraveled to optimize the electronic structures and performance of as-designed electrocatalysts for ORR. Due to the lower electronegativity of Zn, it is easier to donate its outer electron to Fe. The optimized d-band electronic structure leads to the spontaneous filling of the Fermi layer with spin-polarized electrons and promotes their trapping of oxygen-containing intermediates and binding to O_2. As expected, the Fe/Zn-CHNC exhibits exceptional ORR performance in alkaline media, such as a small half-wave potential of 0.91 V, and high stability (only 12 mV loss of half-wave potential after 5,000 LSV scans). Interestingly, the co-presence of Zn and Fe species not only promotes the formation of hollow structures, they can also reduce the adsorption potential of the reaction intermediates. Benefiting from these features, this finding establishes a facile way to obtain diatomic catalysts on a larger scale and can be further applied to the simultaneous atomic dispersion of multiple metals on the substrates, providing valuable insights for the preparation of high-performance and stable diatomic catalysts.

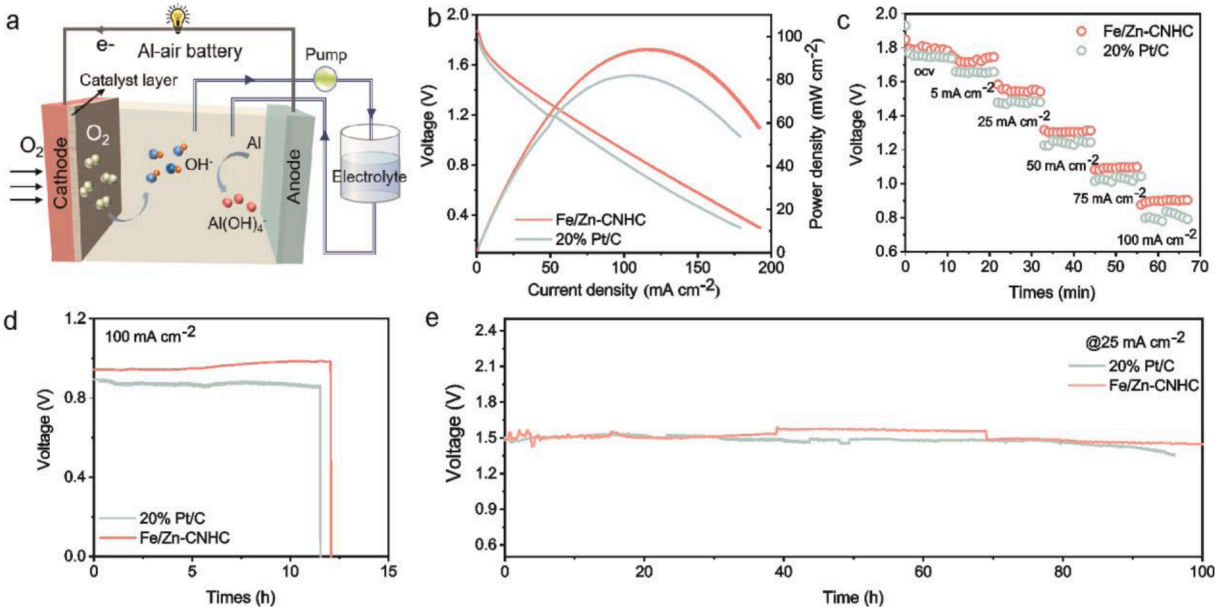

Fig. 6. (a) Diagram of an Al-air battery constructed with Al anode, KOH electrolyte, and as-developed air-cathode; (b) Polarization and power density curves of Al-air batteries with the Fe/Zn-CNHC and Pt/C; (c) The rate discharge performance of the battery with Zn/Fe-CNHC and Pt/C electrodes at various current densities; (d) Discharge curves using Fe/Zn-CNHC and Pt/C at 100 mA cm^{-2}; (e) Discharge tests using the Zn/Fe-CNHC and Pt/C at 25 mA cm^{-2}.

Appendix A. Supporting information

Supplementary data associated with this article can be found in the online vession at doi:10.

CRediT authorship contribution statement

Zheng Li: Conceptualization, Methodology, Formal analysis, Writing – original draft. **Zhongliang Tian:** Conceptualization, Supervision, Funding acquisition, Writing – review & editing. **Hao Cheng:** Investigation, Writing – review & editing. **Tao Wang:** Investigation, Writing – review & editing. **Wei Zhang:** Investigation, Writing – review & editing. **Yao Lu:** Investigation, Writing – review & editing. **Yanqing Lai:** Supervision, Funding acquisition, Writing – review & editing. **Guanjie He:** Conceptualization, Supervision, Funding acquisition, Writing – review & editing.

Declaration of Competing Interest

The authors declare that they have no known competing financial interests or personal relationships that could have appeared to influence the work reported in this paper.

Data availability

Data will be made available on request.

Acknowledgments

The research was supported by the Natural Science Foundation of China (Grants Nos. U20A20280) and the Engineering and Physical Sciences Research Council (EPSRC, EP/V027433/2; EP/Y008707/1).

Supplementary materials

Supplementary material associated with this article can be found, in the online version, at doi:10.1016/j.ensm.2023.04.003.

References

[1] S.S. Shinde, J.Y. Jung, N.K. Wagh, C.H. Lee, D.H. Kim, S.H. Kim, S.U. Lee, J.H. Lee, Ampere-hour-scale zinc–air pouch cells, Nat. Energy 6 (2021) 592–604, https://doi.org/10.1038/s41560-021-00807-8.

[2] G. Yang, J. Zhu, P. Yuan, Y. Hu, G. Qu, B.A. Lu, X. Xue, H. Yin, W. Cheng, J. Cheng, W. Xu, J. Li, J. Hu, S. Mu, J.N. Zhang, Regulating Fe-spin state by atomically dispersed Mn-N in Fe-N-C catalysts with high oxygen reduction activity, Nat. Commun. 12 (2021) 1734, https://doi.org/10.1360/tb-2021-0145.

[3] K. Chen, K. Liu, P. An, H. Li, Y. Lin, J. Hu, C. Jia, J. Fu, H. Li, H. Liu, Z. Lin, W. Li, J. Li, Y.R. Lu, T.S. Chan, N. Zhang, M. Liu, Iron phthalocyanine with coordination induced electronic localization to boost oxygen reduction reaction, Nat. Commun. 11 (2020) 4173, https://doi.org/10.1038/s41467-020-18062-y.

[4] J. Shan, C. Ye, S. Chen, T. Sun, Y. Jiao, L. Liu, C. Zhu, L. Song, Y. Han, M. Jaroniec, Y. Zhu, Y. Zheng, S.Z. Qiao, Short-Range ordered iridium single atoms integrated into cobalt oxide spinel structure for highly efficient electrocatalytic water oxidation, J. Am. Chem. Soc. 143 (2021) 5201–5211, https://doi.org/10.1021/jacs.1c01525.

[5] L. Bai, C.S. Hsu, D.T.L. Alexander, H.M. Chen, X. Hu, Double-atom catalysts as a molecular platform for heterogeneous oxygen evolution electrocatalysis, Nat. Energy (2021), https://doi.org/10.1038/s41560-021-00925-3.

[6] L. Chen, P. Verma, K. Hou, Z. Qi, S. Zhang, Y.S. Liu, J. Guo, V. Stavila, M. D. Allendorf, L. Zheng, M. Salmeron, D. Prendergast, G.A. Somorjai, J. Su, Reversible dehydrogenation and rehydrogenation of cyclohexane and methylcyclohexane by single-site platinum catalyst, Nat. Commun. 13 (2022) 1092, https://doi.org/10.1038/s41467-022-28607-y.

[7] J. Zhao, C. Fu, K. Ye, Z. Liang, F. Jiang, S. Shen, X. Zhao, L. Ma, Z. Shadike, X. Wang, J. Zhang, K. Jiang, Manipulating the oxygen reduction reaction pathway on Pt-coordinated motifs, Nat. Commun. 13 (2022) 685, https://doi.org/10.1038/s41467-022-28346-0.

[8] K.H. Lim, A.S. Lee, V. Atanasov, J. Kerres, E.J. Park, S. Adhikari, S. Maurya, L. D. Manriquez, J. Jung, C. Fujimoto, I. Matanovic, J. Jankovic, Z. Hu, H. Jia, Y. S. Kim, Protonated phosphonic acid electrodes for high power heavy-duty vehicle fuel cells, Nat. Energy (2022), https://doi.org/10.1038/s41560-021-00971-x.

[9] Z. Zhao, C. Chen, Z. Liu, J. Huang, M. Wu, H. Liu, Y. Li, Y. Huang, Pt-Based nanocrystal for electrocatalytic oxygen reduction, Adv. Mater. 31 (2019), e1808115, https://doi.org/10.1002/adma.201808115.

[10] J. Zhang, Y. Yuan, L. Gao, G. Zeng, M. Li, H. Huang, Stabilizing Pt-Based electrocatalysts for oxygen reduction reaction: fundamental understanding and design strategies, Adv. Mater. 33 (2021), e2006494, https://doi.org/10.1002/adma.202006494.

[11] H.F. Wang, L. Chen, H. Pang, S. Kaskel, Q. Xu, MOF-derived electrocatalysts for oxygen reduction, oxygen evolution and hydrogen evolution reactions, Chem. Soc. Rev. 49 (2020) 1414–1448, https://doi.org/10.1039/c9cs00906j.

[12] J. Wang, Y. Gao, H. Kong, J. Kim, S. Choi, F. Ciucci, Y. Hao, S. Yang, Z. Shao, J. Lim, Non-precious-metal catalysts for alkaline water electrolysis: operando characterizations, theoretical calculations, and recent advances, Chem. Soc. Rev. 49 (2020) 9154–9196, https://doi.org/10.1039/d0cs00575d.

[13] C.X. Zhao, J.N. Liu, J. Wang, D. Ren, B.Q. Li, Q. Zhang, Recent advances of noble-metal-free bifunctional oxygen reduction and evolution electrocatalysts, Chem. Soc. Rev. (2021), https://doi.org/10.1039/d1cs00135c.

[14] J. Yaling, Z. Xue, J. Yang, Q. Liu, J. Xian, Y. Zhong, Y. Sun, X. Zhang, Q. Liu, D. Yao, G. Li, Tailoring the electronic structure of atomically dispersed Zn electrocatalyst by coordination environment regulation for high selectivity oxygen reduction, Angew. Chem. Int. Ed. (2021), https://doi.org/10.1002/anie.202110838.

[15] L. Yang, X. Zhang, L. Yu, J. Hou, Z. Zhou, R. Lv, Atomic Fe-N_4 /C in flexible carbon fiber membrane as binder-free air cathode for Zn-air batteries with stable cycling over 1000 hours, Adv. Mater. (2021), e2105410, https://doi.org/10.1002/adma.202105410.

[16] F. Dong, M. Wu, Z. Chen, X. Liu, G. Zhang, J. Qiao, S. Sun, Atomically dispersed transition metal-nitrogen-carbon bifunctional oxygen electrocatalysts for zinc-air batteries: recent advances and future perspectives, Nano Micro Lett. (14) (2022) 36, https://doi.org/10.1007/s40820-021-00768-3.

[17] M. Zhao, H. Liu, H. Zhang, W. Chen, H. Sun, Z. Wang, B. Zhang, L. Song, Y. Yang, C. Ma, Y. Han, W. Huang, A pH-universal ORR catalyst with iron single-atom sites derived from double-layer MOF: superior flexible quasi-solid-state rechargeable Zn-air batteries, Energy Environ. Sci. (2021), https://doi.org/10.1039/d1ee01602d.

[18] J. Wu, Q. Zhang, K. Shen, R. Zhao, W. Zhong, C. Yang, H. Xiang, X. Li, N. Yang, Modulating interband energy separation of boron-doped Fe_7S_8/FeS_2 electrocatalysts to boost alkaline hydrogen evolution reaction, Adv. Funct. Mater. 32 (2021), https://doi.org/10.1002/adfm.202107802.

[19] X. Fu, G. Jiang, G. Wen, R. Gao, S. Li, M. Li, J. Zhu, Y. Zheng, Z. Li, Y. Hu, L. Yang, Z. Bai, A. Yu, Z. Chen, Densely accessible Fe-Nx active sites decorated mesoporous-carbon-spheres for oxygen reduction towards high performance aluminum-air flow batteries, Appl. Catal. B: Environ. 293 (2021), https://doi.org/10.1016/j.apcatb.2021.120176.

[20] Y. Chen, S. Ji, Y. Wang, J. Dong, W. Chen, Z. Li, R. Shen, L. Zheng, Z. Zhuang, D. Wang, Y. Li, Isolated single iron atoms anchored on N-Doped porous carbon as an efficient electrocatalyst for the oxygen reduction reaction, Angew. Chem. Int. Ed. 56 (2017) 6937–6941, https://doi.org/10.1002/anie.201702473.

[21] Y. Chen, Z. Li, Y. Zhu, D. Sun, X. Liu, L. Xu, Y. Tang, Atomic Fe dispersed on N-Doped carbon hollow nanospheres for high-efficiency electrocatalytic oxygen reduction, Adv. Mater. 31 (2019), e1806312, https://doi.org/10.1002/adma.201806312.

[22] X. Fu, R. Gao, G. Jiang, M. Li, S. Li, D. Luo, Y. Hu, Q. Yuan, W. Huang, N. Zhu, L. Yang, Z. Mao, J. Xiong, A. Yu, Z. Chen, Z. Bai, Evolution of atomic-scale dispersion of FeNx in hierarchically porous 3D air electrode to boost the interfacial electrocatalysis of oxygen reduction in PEMFC, Nano Energy 83 (2021), https://doi.org/10.1016/j.nanoen.2020.105734.

[23] C.C. Hou, L. Zou, L. Sun, K. Zhang, Z. Liu, Y. Li, C. Li, R. Zou, J. Yu, Q. Xu, Single-atom iron catalysts on overhang-eave carbon cages for high-performance oxygen reduction reaction, Angew. Chem. Int. Ed. 59 (2020) 7384–7389, https://doi.org/10.1002/anie.202002665.

[24] M. Xiao, Y. Chen, J. Zhu, H. Zhang, X. Zhao, L. Gao, X. Wang, J. Zhao, J. Ge, Z. Jiang, S. Chen, C. Liu, W. Xing, Climbing the Apex of the ORR volcano plot via binuclear site construction: electronic and geometric engineering, J. Am. Chem. Soc. 141 (2019) 17763–17770, https://doi.org/10.1021/jacs.9b08362.

[25] L. Gao, X. Li, Z. Yao, H. Bai, Y. Lu, C. Ma, S. Lu, Z. Peng, J. Yang, A. Pan, H. Huang, Unconventional p-d hybridization interaction in PtGa ultrathin nanowires boosts oxygen reduction electrocatalysis, J. Am. Chem. Soc. 141 (2019) 18083–18090, https://doi.org/10.1021/jacs.9b07238.s001.

[26] H. Li, S. Di, P. Niu, S. Wang, J. Wang, L. Li, A durable half-metallic diatomic catalyst for efficient oxygen reduction, Energy Environ. Sci. (2022), https://doi.org/10.1039/d1ee03194e.

[27] Y. Zhou, E. Song, W. Chen, C.U. Segre, J. Zhou, Y.C. Lin, C. Zhu, R. Ma, P. Liu, S. Chu, T. Thomas, M. Yang, Q. Liu, K. Suenaga, Z. Liu, J. Liu, J. Wang, Dual-metal interbonding as the chemical facilitator for Single-atom dispersions, Adv. Mater. 32 (2020), e2003484, https://doi.org/10.1002/adma.202003484.

[28] Y.Q. Zhang, H.B. Tao, J. Liu, Y.F. Sun, J. Chen, B. Hua, T. Thundat, J.L. Luo, A rational design for enhanced oxygen reduction: strongly coupled silver nanoparticles and engineered perovskite nanofibers, Nano Energy 38 (2017) 392–400, https://doi.org/10.1016/j.nanoen.2017.06.006.

[29] J. Yu, J. Li, C.Y. Xu, Q. Li, Q. Liu, J. Liu, R. Chen, J. Zhu, J. Wang, Modulating the d-band centers by coordination environment regulation of single-atom Ni on porous carbon fibers for overall water splitting, Nano Energy 98 (2022), https://doi.org/10.1016/j.nanoen.2022.107266.

[30] X. Zhu, X. Tan, K.H. Wu, S.C. Haw, C.W. Pao, B.J. Su, J. Jiang, S.C. Smith, J. M. Chen, R. Amal, X. Lu, Intrinsic ORR activity enhancement of Pt atomic sites by

engineering the d-Band center via Localcoordination tuning, Angew. Chem. Int. Ed. 60 (2021) 21911–21917, https://doi.org/10.1002/anie.202107790.
[31] H. Yan, Y. Xie, Y. Jiao, A. Wu, C. Tian, X. Zhang, L. Wang, H. Fu, Holey reduced graphene oxide coupled with an Mo_2N-Mo_2C heterojunction for efficient hydrogen evolution, Adv. Mater. 30 (2018), https://doi.org/10.1002/adma.201704156.
[32] Y. Mun, S. Lee, K. Kim, S. Kim, S. Lee, J.W. Han, J. Lee, Versatile strategy for tuning ORR activity of a single Fe-N_4 site by controlling electron-withdrawing/donating properties of a carbon plane, J. Am. Chem. Soc. 141 (2019) 6254–6262, https://doi.org/10.1021/jacs.8b13543.
[33] X. Ao, W. Zhang, Z. Li, J.G. Li, L. Soule, X. Huang, W.H. Chiang, H.M. Chen, C. Wang, M. Liu, X.C. Zeng, Markedly enhanced oxygen reduction activity of single-atom Fe catalysts via integration with Fe nanoclusters, ACS Nano 13 (2019) 11853–11862, https://doi.org/10.1021/acsnano.9b05913.
[34] H.Jin Fan, M. Knez, R. Scholz, K. Nielsch, E. Pippel, D. Hesse, M. Zacharias, U. Gosele, Monocrystalline spinel nanotube fabrication based on the Kirkendall effect, Nat. Mater. 5 (2006) 627–631, https://doi.org/10.1038/nmat1673.
[35] Y. Chen, S. Ji, S. Zhao, W. Chen, J. Dong, W.C. Cheong, R. Shen, X. Wen, L. Zheng, A.I. Rykov, S. Cai, H. Tang, Z. Zhuang, C. Chen, Q. Peng, D. Wang, Y. Li, Enhanced oxygen reduction with single-atomic-site iron catalysts for a zinc-air battery and hydrogen-air fuel cell, Nat. Commun. 9 (2018) 5422, https://doi.org/10.1038/s41467-018-07850-2.
[36] Z. Zhu, H. Yin, Y. Wang, C.H. Chuang, L. Xing, M. Dong, Y.R. Lu, G. Casillas-Garcia, Y. Zheng, S. Chen, Y. Dou, P. Liu, Q. Cheng, H. Zhao, Coexisting single-atomic Fe and Ni Sites on hierarchically ordered porous carbon as a highly efficient ORR electrocatalyst, Adv. Mater. 32 (2020), e2004670, https://doi.org/10.1002/adma.202004670.
[37] Y. Xiong, H. Li, C. Liu, L. Zheng, C. Liu, J. Wang, S. Liu, Y. Han, L. Gu, J. Qian, D. Wang, Single-atom fe catalysts for fenton-like reactions: roles of different N species, Adv. Mater. 34 (2022), 2110653, https://doi.org/10.1002/adma.202110653.
[38] Z. Zeng, L.Y. Gan, H. Bin Yang, X. Su, J. Gao, W. Liu, H. Matsumoto, J. Gong, J. Zhang, W. Cai, Z. Zhang, Y. Yan, B. Liu, P. Chen, Orbital coupling of hetero-diatomic nickel-iron site for bifunctional electrocatalysis of CO_2 reduction and oxygen evolution, Nat. Commun. 12 (2021) 4088, https://doi.org/10.1038/s41467-021-24052-5.
[39] Y. Chen, R. Gao, S. Ji, H. Li, K. Tang, P. Jiang, H. Hu, Z. Zhang, H. Hao, Q. Qu, X. Liang, W. Chen, J. Dong, D. Wang, Y. Li, Atomic-level modulation of electronic density at cobalt single-atom sites derived from metal-organic frameworks: enhanced oxygen reduction performance, Angew. Chem. Int. Ed. 60 (2021) 3212–3221, https://doi.org/10.1002/anie.202012798.
[40] Y. Li, R. Cao, L. Li, X. Tang, T. Chu, B. Huang, K. Yuan, Y. Chen, Simultaneously integrating single atomic cobalt sites and Co_9S_8 nanoparticles into hollow carbon nanotubes as trifunctional electrocatalysts for Zn-Air batteries to drive water splitting, Small (16) (2020), 1906735, https://doi.org/10.1002/smll.201906735.
[41] F. Luo, S. Wagner, I. Onishi, S. Selve, S. Li, W. Ju, H. Wang, J. Steinberg, A. Thomas, U.I. Kramm, P. Strasser, Surface site density and utilization of platinum group metal (PGM)-free Fe–NC and FeNi–NC electrocatalysts for the oxygen reduction reaction, Chem. Sci. (12) (2021) 384–396, https://doi.org/10.1039/D0SC03280H.
[42] H. Wang, X. Li, Y. Jiang, M. Li, Q. Xiao, T. Zhao, S. Yang, C. Qi, P. Qiu, J. Yang, Z. Jiang, W. Luo, A Universal single-atom coating strategy based on tannic acid chemistry for multifunctional heterogeneous catalysis, Angew. Chem. Int. Ed. (61) (2022), e202200465, https://doi.org/10.1002/anie.202200465.
[43] M. Tong, F. Sun, Y. Xie, Y. Wang, Y. Yang, C. Tian, L. Wang, H. Fu, Operando cooperated catalytic mechanism of atomically dispersed Cu-N_4 and Zn-N_4 for promoting oxygen reduction reaction, Angew. Chem. Int. Ed. (60) (2021) 14005–14012, https://doi.org/10.1002/anie.202102053.
[44] Z. Lu, K. Jiang, G. Chen, H. Wang, Y. Cui, Lithium electrochemical tuning for electrocatalysis, Adv. Mater. 30 (2018), e1800978, https://doi.org/10.1002/adma.20180097.
[45] W. Liu, P. Bai, S. Wei, C. Yang, L. Xu, Gadolinium changes the local electron densities of nickel 3d orbitals for efficient electrocatalytic CO_2 reduction, Angew. Chem. Int. Ed. (2022), e202201166, https://doi.org/10.1002/anie.202201166.
[46] H. Cheng, X. Wu, M. Feng, X. Li, G. Lei, Z. Fan, D. Pan, G.He F.Cui, Atomically dispersed Ni/Cu dual sites for boosting the CO_2 reduction reaction, ACS Catal. (11) (2021) 12673–12681, https://doi.org/10.1021/acscatal.1c02319.
[47] H. Li, J. Wang, R. Qi, Y. Hu, J. Zhang, H. Zhao, J. Zhang, Y. Zhao, Enhanced Fe 3d delocalization and moderate spin polarization in Fe Ni atomic pairs for bifunctional ORR and OER electrocatalysis, Appl. Catal. B Environ. 285 (2021), https://doi.org/10.1016/j.apcatb.2020.119778.
[48] H. Xu, D. Cheng, D. Cao, X.C. Zeng, A universal principle for a rational design of single-atom electrocatalysts, Nat. Catal. 1 (2018) 339–348, https://doi.org/10.1038/s41929-018-0063-z.
[49] S. Sun, X. Zhou, B. Cong, W. Hong, G. Chen, Tailoring the d-Band centers endows $(NixFe_{1-x})_2P$ nanosheets with efficient oxygen evolution catalysis, ACS Catal. 10 (2020) 9086–9097, https://doi.org/10.1021/acscatal.0c01273.s001.
[50] X. Han, X. Ling, D. Yu, D. Xie, L. Li, S. Peng, C. Zhong, Y.Deng N.Zhao, W. Hu, Atomically dispersed binary Co-Ni sites in nitrogen-doped hollow carbon nanocubes for reversible oxygen reduction and evolution, Adv. Mater. (31) (2019), 1905622, https://doi.org/10.1002/adma.201905622.
[51] J. Wang, H. Li, S. Liu, Y. Hu, J. Zhang, M. Xia, Y. Hou, J. Tse, J. Zhang, Y. Zhao, Turning on Zn 4s electrons in a N_2-Zn-B_2 configuration to stimulate remarkable ORR performance, Angew. Chem. 133 (2020) 183–187, https://doi.org/10.1002/anie.202009991.
[52] Y Xue, Y Guo, Q Zhang, Z Xie, J Wei, Z Zhou, MOF-derived Co and Fe species loaded on N-doped carbon networks as efficient oxygen electrocatalysts for Zn-Air batteries, Nanomicro Lett. 14 (1) (2022) 162, https://doi.org/10.1007/s40820-022-00890-w.